Research Article Vol. 31, No. 2 / 16 Jan 2023 / Optics Express 3379
Optics EXPRESS

Trajectory-controlled high-order harmonic generation in ZnO crystals

YANG WANG,[1] TIANJIAO SHAO,[2,7] XIAOFANG LI,[1] YU LIU,[1] PENGZUO JIANG,[1] WEI ZHENG,[1] LINFENG ZHANG,[1] XUE-BIN BIAN,[3,8] YUNQUAN LIU,[1,4,5,6] QIHUANG GONG,[1,4,5,6] AND CHENGYIN WU[1,4,5,6,*]

[1]*State Key Laboratory for Mesoscopic Physics and Frontiers Science Center for Nano-Optoelectronics, School of Physics, Peking University, Beijing 100871, China*
[2]*School of Information Science and Engineering, NingboTech University, Ningbo 315100, China*
[3]*State Key Laboratory of Magnetic Resonance and Atomic and Molecular Physics, Wuhan Institute of Physics and Mathematics, Innovation Academy for Precision Measurement Science and Technology, Chinese Academy of Sciences, Wuhan 430071, China*
[4]*Collaborative Innovation Center of Quantum Matter, Beijing 100871, China*
[5]*Collaborative Innovation Center of Extreme Optics, Shanxi University, Taiyuan, Shanxi 030006, China*
[6]*Peking University Yangtze Delta Institute of Optoelectronics, Nantong, Jiangsu 226010, China*
[7]*shaotj@nit.zju.edu.cn*
[8]*xuebin.bian@wipm.ac.cn*
[*]*cywu@pku.edu.cn*

Abstract: We experimentally and theoretically study high-order harmonic generation in zinc oxide crystals irradiated by mid-infrared lasers. The trajectories are mapped to the far field spatial distribution of harmonics. The divergence angles of on-axis and off-axis parts exhibit different dependences on the order of the harmonics. This observation can be theoretically reproduced by the coherent interference between the short and long trajectories with dephasing time longer than 0.5 optical cycle. Further, the relative contribution of the short and long trajectories is demonstrated to be accurately controlled by a one-color or two-color laser on the attosecond time scale. This work provides a reliable method to determine the electron dephasing time and demonstrates a versatile control of trajectory interference in the solid high-order harmonic generation.

1. Introduction

Electrons are the glue of materials and respond to laser fields rapidly. Observing and manipulating the behavior of electrons on the sub-femtosecond time scale is one of the hearts of ultrafast science [1–5]. Advancements in laser technologies have allowed us to extend electron metrology to the multi-petahertz range [6]. At the same time, coherent high-order harmonic (HH) photons are emitted when strong lasers interact with atoms, molecules, and condensed matter. HH and its sidebands offer a powerful platform for exploring the dynamics of microscopic particles with subcycle temporal resolutions [7–9]. In 2011, Ghimire *et al*. reported the observation of non-perturbative HH in ZnO bulk crystals [10], which opened the door to the research of solid high-order harmonic generation (HHG). Up to now, solid HH has been observed in wide-bandgap crystals [11,12], metamaterials [13–15], atomically thin materials [16–19], topological materials [20], and semi-metallic materials [21–24]. In principle, the mechanism can be divided into intraband mechanism and interband mechanism. The former is caused by the strong laser field-driven electron dynamic oscillation in individual bands. The latter is a result of interband polarization between electrons and holes, analogous to the extensively studied gas HHG in the past few decades [25–28]. It has been confirmed that the HHG in GaSe single crystals driven

#481744 https://doi.org/10.1364/OE.481744
Journal © 2023 Received 23 Nov 2022; revised 31 Dec 2022; accepted 2 Jan 2023; published 13 Jan 2023

Optics EXPRESS

by a THz laser originates from nonlinear intraband currents [29], while the HHG in sapphire single crystals is believed to originate from interband polarization [30]. Due to the complexities of solid materials, the dominating mechanism is still under debate. A typical example is HH in ZnO. It is thought to be derived from the intraband contribution, which explains the unique linear scale of high-energy cutoff with drive-laser field strength [10]. Nonetheless, the pump-probe measurement in Ref. [31] indicates that the interband polarization is the primary origin. Novel experimental data are helpful to determine the microscopic genesis of solid HHG.

The structure of HH spectrum contains abundant information regarding ultrafast electron motion, from which the trajectory-resolved dynamics has been successfully extracted in gas HHG [27,28,32]. The extraction of such information relies on the direct comparison of experimental measurements and theoretical simulations. However, the semiconductor Bloch equation (SBE) simulation, one of the most important numerical approaches for studying solid HHG, is sensitive to the obscure dephasing time. The reliable trajectory-resolved analysis of solid HHG cannot be performed due to the lack of knowledge of the dephasing time. A short dephasing time is commonly used to obtain a high-resolution HH spectrum, but the underestimating of this time may inevitably lead to the artificial destruction of ultrafast electron dynamics. Unfortunately, it is extremely difficult to deduce the origin of dephasing time and determine its magnitude, which may include the tricky many-body effect. The value of the dephasing time is widely believed to be around a quarter of an optical cycle (o.c.) [33]. An isolated attosecond pulse is required to directly measure the dephasing time, which is only available in few laboratories [34]. Very recently, this time is extracted in an atomically thin semiconductor by photodoping incoherent electron–hole pairs [35]. Discovering the indirect relationship between dephasing time and experimental observable quantity is likely a deft solution to the dilemma. Determining the dephasing time paves the way for reliable trajectory-resolved analysis of solid HHG. Controlling the trajectory-resolved interference is crucial for comprehending the origin of solid HHG [24,30,36–39], elucidating its relationship with gas HHG [40], and promoting solid HHG application in the establishment of advanced laser sources and material characterization [41–46].

In this work, we imaged the far-field divergence angle of HH in ZnO crystals by spatial filtering. In conjunction with theoretical simulations, it is revealed that the interband polarization dominates the contribution to the harmonics above the bandgap. More importantly, we determined the magnitude of the dephasing time using a reliable method that is easy to realize in laboratory. Further, we demonstrate that the trajectory interference for HH in ZnO can be controlled by the shape of the driving laser field. The parallel two-color laser can precisely tune ultrafast electron interference between long and short trajectories, resulting in a rich interference structure in the frequency domain. Our work sheds light on the value of electron dephasing time and modulation of trajectory interference in solid HHG.

2. Methods

2.1. Experimental scheme

Figure 1 shows the schematic diagram of the experimental setup. A mid-infrared laser (MIR) with center wavelength of about 3.5 μm and pulse duration of about 150 fs is generated through the collinear difference frequency between the signal and idler beams of a femtosecond optical parametric amplifier (OPA). The second harmonic of the MIR is generated in a $AgGaS_2$ (AGS) crystal right after the pin-hole to improve laser mode quality, where the crystal and pin-hole are placed in a focusing and collimating system consisting of two symmetrical off-axis parabolic mirrors. The fundamental and second harmonic lasers are separated and recombined to precisely control their relative phases by a Michelson interferometer configuration, including a nanoscale precision delay line. Finally, the MIR and its second harmonic are focused into the ZnO single crystal (0001 crystal orientation, 350 μm thickness) by an off-axis parabolic mirror. The laser intensity can be adjusted continuously by a combination of a half-wave plate and a linear polarizer.

Optics EXPRESS

The HHs are spatially filtered by a scannable slit with 1 mrad acceptance angle and then focused by a MgF_2 lens into a spectrometer for spectral analysis. When the AGS crystal was removed from the optical path, the same optical setup was used to perform the HHG experiment with a one-color laser. The laser field strength is calibrated by comparing the theoretical simulation and experimental observation.

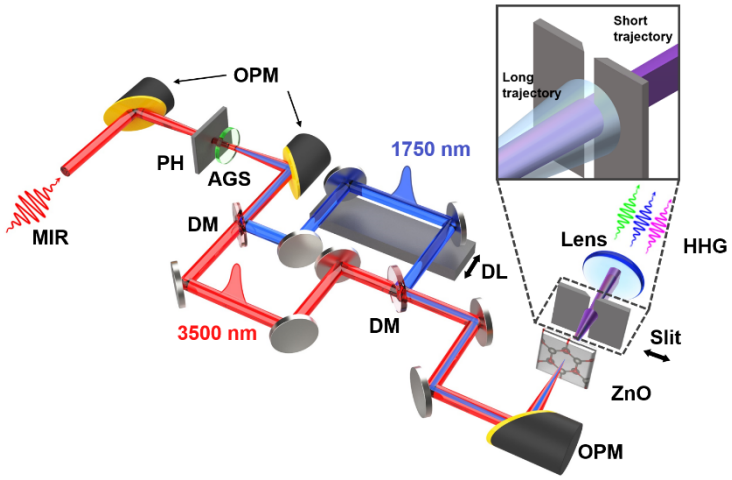

Fig. 1. Schematic diagram of the experimental setup. MIR, Mid-infrared laser; PH, pin-hole; AGS, $AgGaS_2$ crystal; DM, dichroic mirror; DL, delay line; Slit, spatial filtering slit; Lens, MgF_2 lens. The inset is a schematic diagram of trajectory-resolved measurement by spatial filtering.

2.2. Theoretical method

The electron/hole dynamics in the crystal driven by the strong laser is modeled by the reciprocal k-space semiconductor Bloch equation (SBE). The two-band model is expressed as follows [33,47],

$$\dot{\pi}(K,t) = -\frac{\pi(K,t)}{T_2} - i\Omega(K,t)w(K,t)e^{-iS(K,t)} \tag{1a}$$

$$\dot{n}_b(K,t) = is_b\Omega^*(K,t)\pi(K,t)e^{iS(K,t)} + c.c. \tag{1b}$$

where $\pi(K,t)$ represents the polarization strength between the conduction band (CB) and valence band (VB), and $n_b(K,t)$ denotes the conduction and valence band population. The Rabi frequency is expressed as $\Omega(K,t) = d(K + A(t))E(t)$. The population difference is expressed as follows, $w(K,t) = n_V(K,t) - n_C(K,t)$. The distinguish factor S_b is given by, S_b =1 (CB) and -1 (VB), respectively. $S(K,t) = \int_{-\infty}^{t} \varepsilon_g(K + A(t'))dt'$ is the classical action, ε_g is the band gap, and T_2 is the dephasing time.

The intracurrent (j_{ra}) and intercurrent (j_{er}) can be obtained by solving the SBE,

$$j_{ra}(t) = \sum\nolimits_{b=c,v} \int_{\overline{BZ}} v_b[K + A(t)]n_b(K,t)d^3K \tag{2a}$$

$$j_{er}(t) = \frac{d}{dt}\int_{\overline{BZ}} p(K,t)d^3K \tag{2b}$$

where $v_b[K + A(t)]$ is defined as the band velocity, an $p(K,t) = d(K + A(t))\pi(K,t)e^{iS(K,t)} + c.c.$ is the polarization. It should be noted, the above integration in Eqs. (2a) and (2b) is taken over the whole first Brillouin zone ($\overline{BZ}$). Our calculation is carried out along the one-dimensional

Optics EXPRESS

path along the polarization direction of the linearly polarized driving laser. The interband contribution $|FT\{j_{er}(t)\}|^2$ and intraband contribution $|FT\{j_{ra}(t)\}|^2$ to the HHG can be obtained separately from the Fourier transform (FT) of $j_{er}(t)$ an $j_{ra}(t)$. The total HHG spectra is obtained by $|\mathrm{FT}\{j_{tot}(t)\}|^2$, where $j_{tot}(t) = j_{er}(t) + j_{ra}(t)$. Our simulation indicates that interband contribution is about two orders of magnitude higher than the intraband contribution for the above-bandgap harmonics. Therefore, the intraband contribution is not included in our theoretical simulation.

Under the Keldysh approximation ($w(K,t) \approx 1$), the $j_{er}(t)$ can be expressed as follows [33,47],

$$j_{er}(t) = \frac{d}{dt} \int_{BZ} d^3K d(K) \left[\int_{-\infty}^{t} dt' E(t') d^*(K + A(t')) e^{iS(K,t',t) - \frac{t-t'}{T_2}} + c.c. \right] \tag{3}$$

Then in the frequency domain, the HHG contributed by the interband current can be written as,

$$j_{er}(\omega) = \omega \int_{BZ} d^3K d(K) \int_{-\infty}^{\infty} dt e^{-i\omega t} \left[\int_{-\infty}^{t} dt' E(t') d^*(K + A(t')) e^{iS(K,t',t) - \frac{t-t'}{T_2}} + c.c. \right] \tag{4}$$

The phase term of the HH photon is given by,

$$i\phi = iS(K,t,t') - i\omega t - \frac{t-t'}{T_2} \tag{5}$$

Using the saddle-point method,

$$\nabla_k \phi = \int_{t'}^{t} \Delta v(K - A(t) + A(t'')) dt'' = 0 \tag{6a}$$

$$\frac{d\phi}{dt'} = \varepsilon_g[K - A(t) + A(t')] - \frac{i}{T_d} = 0 \tag{6b}$$

$$\frac{d\phi}{dt} = \varepsilon_g(K) - \omega + \frac{i}{T_d} = 0 \tag{6c}$$

where $\Delta v(K) = v_c(K) - v_v(K)$ in Eq. (6a) is the band velocity difference between the conduction band and valence band. By solving Eqs. (6a) to (6c), the classical trajectory of the interband transition can be traced, the dependence of the HH photon energy ω on the ionization time t_i and recombination time t_r can be obtained.

3. Results and discussion

Figure 2 presents the far-field distribution of harmonics obtained from the experiment and simulation. In Fig. 2(a), the measured above-bandgap HH spectrum exhibits two far-field spatial parts, corresponding to large and small divergence angles. The on-axis part has a small divergence angle that is approximately constant with the harmonic order. In contrast, the off-axis part has a large divergence angle, which decreases with the increase of the harmonic order and exhibits an arrow-like shape. Such far-field distribution has been observed in the gas HHG and has been applied to distinguish the contribution of different trajectories to the harmonic yield [32,48]. In solid HHG, some theoretical works predicted that harmonic radiation at different times may lead to the harmonic radiation with different divergence angles [49,50]. Here, we demonstrate that the dephasing time, one of the most important parameters in the theoretical simulation of solid HHG [47], can be determined for the first time through the comparison between the measured far-field HH spectrum and theoretical simulation with different dephasing times. Figures 2(b) and 2(c) show the simulated far-field spectra for dephasing time $T_2 = 0.500$ o.c. and 0.167 o.c. with the electric field E being 0.0030 a.u. Figure 2(b) reproduces the experimental observation, both on-axis and off-axis parts are obvious. In Fig. 2(c), the off-axis part disappears because a shorter dephasing time is applied and suppresses the contribution of long trajectories. The contribution

Optics EXPRESS

of the short trajectories to the harmonic radiation mainly distributed along the axis. The phase accumulation of different quantum trajectories can be mapped to the far-field divergence angle of harmonics through propagation. Dephasing time modulates the far-field distribution of HH by determining the survived trajectory. Thus, the far-field distribution can be served as a sensitive probe of the dephasing time. By the combination of theoretical simulations with experimental measurements, far-field HH spectrum provides a reliable way to determine the dephasing time. This method is not restricted by the limitation of the time resolution of the driver laser. It relies on the spatial resolution, which can be easily achieved in the laboratory. Using this method, the HHG dephasing time of ZnO bulk is determined to be 0.500 o.c., which is twice as long as the value taken in the earlier theoretical research [33]. Spatial-integral HH spectrum is often used to determine dephasing time by comparison with theoretical simulation. However, this method is more suitable for the condition that the HH spectrum has some typical features, such as the appearance of spectral peak splitting. The presented spatial-resolved HH spectrum can quantitatively determine the dephasing time by measuring the divergence angle. In the following experiments, we measured the spatial-integral HH spectrum. The theoretically simulated HH spectrum reproduced the spectral peak splitting by using the dephasing time determined by the spatial-resolved HH spectrum. These results agree with each other and demonstrate that the dephasing time determined by far-field filtering method is reliable.

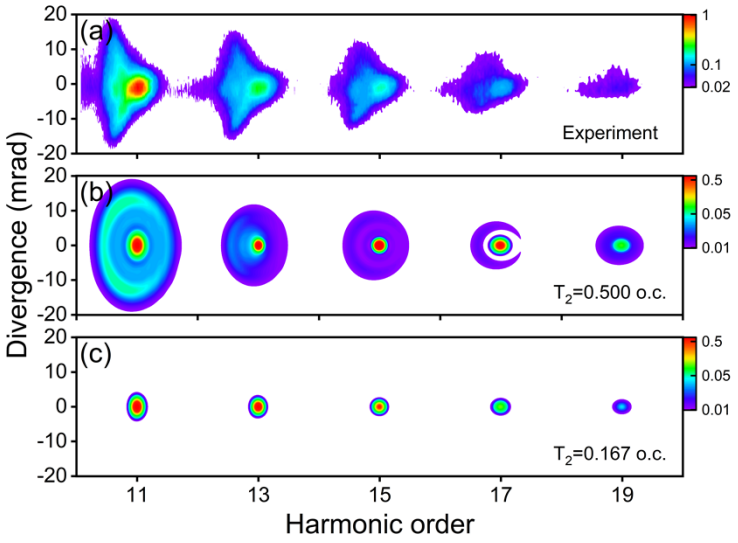

Fig. 2. Far-field harmonic spectra in ZnO. (a) Experimental measurement, (b) theoretical simulation with dephasing time $T_2 = 0.500$ o.c. and (c) $T_2 = 0.167$ o.c. The color diagram represents the normalized harmonic yields. Simulated laser parameters: wavelength $\lambda = 3600$ nm, pulse duration $\tau = 150$ fs, field strength $E_0 = 0.0030$ a.u.

In addition, the spatial-resolved HH spectrum indicates that above-bandgap harmonics mainly come from the interband polarization under our experimental condition because the spatial divergence angle of intraband harmonics decreases sharply with the harmonic order [50], which is inconsistent with our experimental observation. This result is in line with our prediction in the theoretical method section by separating the intraband and interband contributions. The far-field distribution of harmonics contains the characteristic fingerprint. It provides evidence for revealing the generation mechanism of solid HH and experimental reconstruction of the ultrafast electron dephasing time, while these potentials have not been fully exploited in previous studies of spatially distributed HH spectra [51].

Optics EXPRESS

The long dephasing time makes multiple quantum trajectories coexist. The phase difference between different trajectories is influenced by the laser intensity. Therefore, the shape of the HH spectrum depends on the interference between quantum trajectories as well as the laser intensity. Indeed, the HH peaks become broadening and splitting when the laser intensity increases, as shown in Fig. 3(a). Reflection harmonic spectrum is also measured as shown in Fig. 3(b), in which the nonlinear propagation effect is eliminated [52]. The qualitative consistency between the reflection and transmission harmonic spectrum indicates that peak splitting is not from nonlinear propagation of the laser. Figures 3(c) and 3(d) show the calculated harmonic spectra (left panel) and time-frequency analysis (right panel) with dephasing time $T_2 = 0.500$ o.c. and $T_2 = 0.167$ o.c., respectively. When the dephasing time T_2 is taken as 0.500 o.c., the time-frequency analysis shows that both short and long trajectories contribute to harmonics. The calculated harmonic spectrum reproduces the main characteristics of the experimental observation at high laser intensity, the peak broadening and splitting. With T_2 changing from 0.500 o.c. to 0.167 o.c., the long trajectory is almost completely suppressed. The narrow odd-order harmonic spectrum without any splitting indicates that the broadening and splitting of the harmonic spectrum come from the interference between long and short trajectories. Figure 3(d) also implies that the peak splitting is not caused by the interference between short trajectories of different optical cycles. The long dephasing time makes both the long and short trajectories contribute to harmonic generation even driven by long wavelength laser. The relative contribution of the long and short trajectories can be controlled by adjusting the laser intensity. This modulation method requires laser intensity changes in a wide range. However, the maximum laser intensity in solid HHG is limited by the material damage threshold and the laser nonlinear propagation effect.

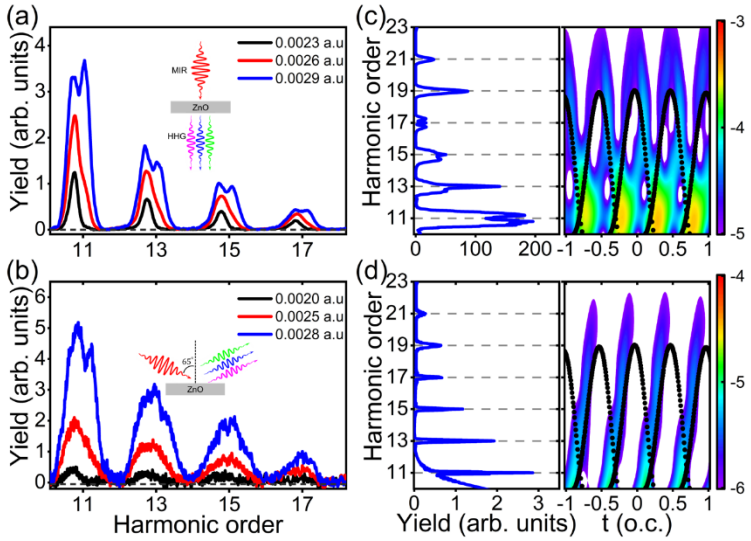

Fig. 3. High harmonic spectra in ZnO driven by a one-color laser field. Experimental measured harmonic spectra with various field strengths in the transmission **(a)** and reflection **(b)** modes. The inset is a schematic diagram of harmonic emission. Calculated harmonic spectra (left panel) and time-frequency analysis (right panel) with dephasing time $T_2 = 0.500$ o.c. **(c)** and $T_2 = 0.167$ o.c. **(d)**. The black scatters represent the semi-classical harmonic energy as a function of emission time. Simulated laser parameters: wavelength $\lambda = 3600$ nm, pulse duration $\tau = 150$ fs, field strength $E_0 = 0.0030$ a.u.

Next we turn to explore the trajectory-controlled HHG in ZnO using a synthetic laser field, which offers a powerful platform for controlling electron motion without introducing extra

Optics EXPRESS

propagation effect of a strong one-color laser field [53]. The typical synthetic laser field consists of a fundamental laser and its second harmonic (SH). The two-color laser field breaks inversion symmetry and even leads to a single HHG shutter in one optical cycle. Here, we use a parallel two-color laser field with a weak SH to demonstrate the trajectory-controlled HHG in ZnO crystal. Figure 4(a) shows the HH spectra as a function of the time delay between the two laser pulses. The SH breaks the inversion symmetry and produces a spectrum containing even and odd harmonics. The harmonic yields oscillate periodically at four times the fundamental laser frequency. Different from previous two-color laser scheme with the time delay as the control parameter [54,55], the time delay is fixed at 0.500 π and the intensity of weak SH is used as a control knob in the present control scheme. Figure 4(b) shows the HH spectra at three different k values, where k represents the intensity ratio of SH to the fundamental laser. When k surpasses 1.0%, the peak of 11th harmonic becomes wider and exhibits a splitting fringe pattern. The result indicates that the present two-color laser field is a highly sensitive manipulation scheme and extra nonlinear propagation effects are not introduced due to the little change of the total laser intensity in ZnO. We also performed a numerical simulation of SBE with various k values. As illustrated in Fig. 4(c), the theoretical simulation reproduces the experimental trend for the spectral broadening and splitting of 11th harmonic with the increase of k value. Figure 4(d) provides detailed simulation results, including the individual contributions of short (red dotted line) and long trajectories (blue dotted line) filtered by a Hanning window function. The coherent superposition spectrum profile from short and long trajectories clearly reproduces the measured spectral shape. The result provides another evidence that the modulated spectral splitting and broadening observed from the 11th harmonic peak come from the interference between short and long trajectories, and this interference can be sensitively controlled by a parallel two-color laser field.

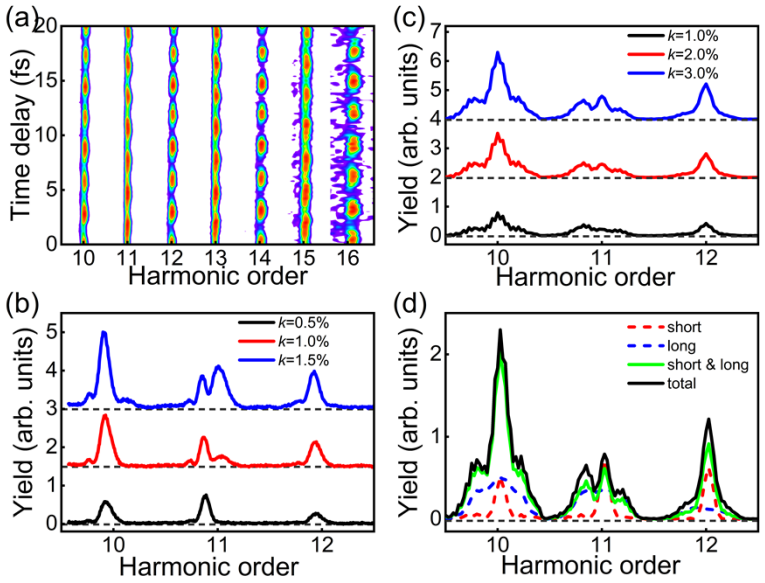

Fig. 4. Harmonic spectra in ZnO driven by a two-color laser field. **(a)** Measured harmonic yield oscillates periodically with the relative phase of the two lasers. **(b)** The shape of the harmonic spectrum is controlled by the SH intensity with the relative phase is 0.500π. **(c)** Calculated harmonic spectra with $T_2 = 0.500$ o.c. **(d)** Absolute amplitudes of interband polarization for long, short trajectories, their coherent superposition, and total contribution of SBE with $k = 3.0\%$. Simulated laser parameters: wavelength $\lambda = 3500$ nm, pulse duration $\tau = 150$ fs, field strength $E_0 = 0.0020$ a.u., relative phase $\Phi r = 0.500\pi$.

Optics EXPRESS

The windowed Fourier transform and the semi-classical analysis provide more insight into the coherent manipulation. Figure 5 presents the temporal profiles of HHG with different k values. The black scatters represent photon energy as a function of the birth time of electron-hole pair obtained by the saddle point analysis. The color diagram represents the recombination time of electron-hole pair, where HHs are emitted. The birth times of electron-hole pairs form an effective harmonic excitation window with the rising (falling) edge corresponding to the long (short) trajectories. The recombination times of electron-hole pairs form a harmonic emission window, which is around half optical cycle after the harmonic excitation window. The solid red line represents the time-dependent electron excitation rates and forms an electron excitation window. In Fig. 5(a), $k = 0$ corresponds to the one-color laser field, the subcycle harmonic emission repeats in each half optical cycle. It is similar to a balanced time-domain Michelson interferometer with two arms consisting of harmonic emissions in consecutive half cycles. All even harmonics vanish due to the temporal symmetry. As k grows, the temporal symmetry is broken. The waveform of the two-color laser field changes both the electron excitation window and the harmonic excitation window. The contribution from adjacent half cycles is not equal anymore. As shown in Figs. 5(b-d), every optical cycle can be divided into one strong half cycle and one weak half cycle, which are respectively marked by solid and dashed rectangles. In the strong half cycle, such as $t = 0.500$ o.c., the electron excitation window matches with the harmonic excitation window better and the harmonic yield increases. Instead in the weak half cycle, such as $t = 0$ o.c., the two windows do not match and the harmonic yield reduces. The reduction does not mean that the absolute number of excited electrons decreases in the weak half cycle. Instead, these electrons cannot efficiently recombine with the associated hole, resulting in the reduction of the harmonic yield.

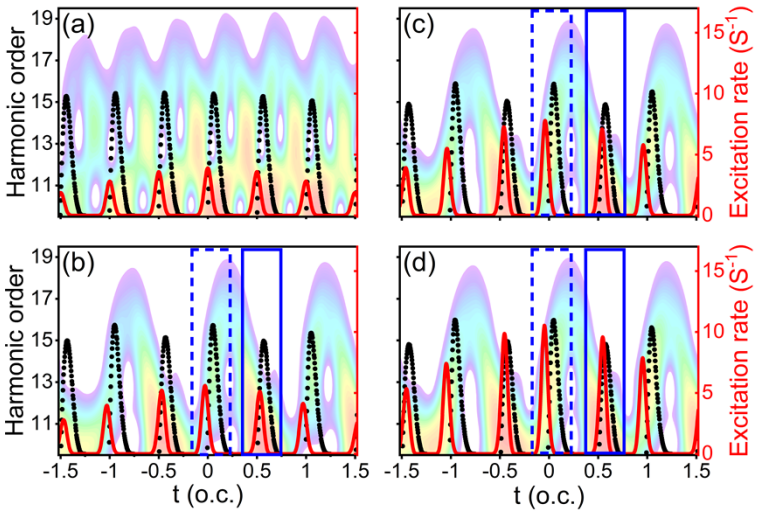

Fig. 5. Second harmonic laser intensity effect on spectrograph modulation. (a) $k = 0$. (b) $k = 1.0\%$. (c) $k = 2.0\%$. (d) $k = 3.0\%$. Black scatters show photon energy as a function of excitation times from the saddle-point analysis. The color diagrams show the photon energy as a function of the recombination times, and different colors are used to describe their respective normalized harmonic yields. The solid red line represents the time-dependent excitation rates. The fundamental laser parameters are the same as those in Fig. 4.

Further, we explore the subcycle interference between short and long trajectories in a strong half cycle. When $k = 0$, the electron excitation window coincides with the harmonic excitation window of the long trajectory. As a result, the contribution of long trajectories is dominant.

Optics EXPRESS

As k increases, the increased electric field enhances the contribution of both the long and short trajectories. However, the contribution of short trajectories increases faster than the long trajectories, which modulates the equivalent interferometer in the same half cycle. By comparing the electron excitation window and harmonic excitation window from the saddle-point analysis, the electron excitation window moves monotonously from the long trajectory branch to the short one as k increases, until the long and short trajectories have the same contribution to make the interference stronger. In fact, the dephasing time induced by electron scattering suppresses the contribution of long trajectories more than that of short trajectories since these carriers travel longer in real space. In the experiment, although the total laser intensity varies less than 2.0% and the time shift of the excitation window is less than 600 as, the harmonic spectral shape produces significant modulation, demonstrating the extremely high sensitivity of the two-color control scheme.

4. Conclusions

In summary, our study builds a bridge between the time and space domain of HHG through far-field spatial filtering. It allows not only the separation of short and long trajectories to the harmonic contribution, but also the determination of electron dephasing time. Moreover, precise control of ultrafast electron interference between the long and short trajectories is demonstrated by using a two-color synthetic laser field. The slight variation of the SH intensity can modulate the harmonic optical frequency comb and the relative contribution of the long and short trajectories, presenting detectable interference fringes in the frequency domain. Our theoretical simulation reproduces all experimental observations and provides solid evidences of the quantum interference between the short and long trajectories from interband transitions. Our work provides a reliable experimental means to determine the magnitude of dephasing time in solid. It paves the way for accurately extracting ultrafast electron dynamics in condensed matter by HHG and extending information science to the multi-petahertz range through controlling ultrafast electron trajectory interference.

Funding. National Key Research and Development Program of China (2018YFA0306302); National Natural Science Foundation of China (12174011, 12104395, 92250305, 11625414); Natural Science Foundation of Zhejiang Province (LQ22A040004).

Disclosures. The authors declare no conflicts of interest.

Data Availability. All the data used in this study are available on request from the corresponding authors.

References

1. P. Gaal, W. Kuehn, K. Reimann, M. Woerner, T. Elsaesser, and R. Hey, "Internal motions of a quasiparticle governing its ultrafast nonlinear response," Nature **450**(7173), 1210–1213 (2007).
2. A. L. Cavalieri, N. Müller, T. Uphues, V. S. Yakovlev, A. Baltuška, B. Horvath, B. Schmidt, L. Blümel, R. Holzwarth, S. Hendel, M. Drescher, U. Kleineberg, P. M. Echenique, R. Kienberger, F. Krausz, and U. Heinzmann, "Attosecond spectroscopy in condensed matter," Nature **449**(7165), 1029–1032 (2007).
3. A. Schiffrin, T. Paasch-Colberg, N. Karpowicz, V. Apalkov, D. Gerster, S. Mühlbrandt, M. Korbman, J. Reichert, M. Schultze, S. Holzner, J. V. Barth, R. Kienberger, R. Ernstorfer, V. S. Yakovlev, M. I. Stockman, and F. Krausz, "Optical-field-induced current in dielectrics," Nature **493**(7430), 70–74 (2013).
4. M. Lucchini, S. A. Sato, A. Ludwig, J. Herrmann, M. Volkov, L. Kasmi, Y. Shinohara, K. Yabana, L. Gallmann, and U. Keller, "Attosecond dynamical Franz-Keldysh effect in polycrystalline diamond," Science **353**(6302), 916–919 (2016).
5. F. Schlaepfer, M. Lucchini, S. A. Sato, M. Volkov, L. Kasmi, N. Hartmann, A. Rubio, L. Gallmann, and U. Keller, "Attosecond optical-field-enhanced carrier injection into the GaAs conduction band," Nat. Phys. **14**(6), 560–564 (2018).
6. M. Garg, M. Zhan, T. T. Luu, H. Lakhotia, T. Klostermann, A. Guggenmos, and E. Goulielmakis, "Multi-petahertz electronic metrology," Nature **538**(7625), 359–363 (2016).
7. M. Hohenleutner, F. Langer, O. Schubert, M. Knorr, U. Huttner, S. W. Koch, M. Kira, and R. Huber, "Real-time observation of interfering crystal electrons in high-harmonic generation," Nature **523**(7562), 572–575 (2015).

Optics EXPRESS

8. F. Langer, M. Hohenleutner, C. P. Schmid, C. Poellmann, P. Nagler, T. Korn, C. Schüller, M. S. Sherwin, U. Huttner, J. T. Steiner, S. W. Koch, M. Kira, and R. Huber, "Lightwave-driven quasiparticle collisions on a subcycle timescale," Nature **533**(7602), 225–229 (2016).
9. F. Langer, C. P. Schmid, S. Schlauderer, M. Gmitra, J. Fabian, P. Nagler, C. Schüller, T. Korn, P. G. Hawkins, J. T. Steiner, U. Huttner, S. W. Koch, M. Kira, and R. Huber, "Lightwave valleytronics in a monolayer of tungsten diselenide," Nature **557**(7703), 76–80 (2018).
10. S. Ghimire, A. D. DiChiara, E. Sistrunk, P. Agostini, L. F. DiMauro, and D. A. Reis, "Observation of high-order harmonic generation in a bulk crystal," Nat. Phys. **7**(2), 138–141 (2011).
11. Y. S. You, D. A. Reis, and S. Ghimire, "Anisotropic high-harmonic generation in bulk crystals," Nat. Phys. **13**(4), 345–349 (2017).
12. L. Li, Y. Zhang, P. Lan, T. Huang, X. Zhu, C. Zhai, K. Yang, L. He, Q. Zhang, and W. Cao, "Dynamic Core Polarization in High Harmonic Generation from Solids: The Example of MgO Crystals," Phys. Rev. Lett. **126**(18), 187401 (2021).
13. S. Han, H. Kim, Y. W. Kim, Y.-J. Kim, S. Kim, I.-Y. Park, and S.-W. Kim, "High-harmonic generation by field enhanced femtosecond pulses in metal-sapphire nanostructure," Nat. Commun. **7**(1), 13105 (2016).
14. H. Liu, C. Guo, G. Vampa, J. L. Zhang, T. Sarmiento, M. Xiao, P. H. Bucksbaum, J. Vučković, S. Fan, and D. A. Reis, "Enhanced high-harmonic generation from an all-dielectric metasurface," Nat. Phys. **14**(10), 1006–1010 (2018).
15. M. Sivis, M. Taucer, G. Vampa, K. Johnston, A. Staudte, Y. Naumov Andrei, D. M. Villeneuve, C. Ropers, and P. B. Corkum, "Tailored semiconductors for high-harmonic optoelectronics," Science **357**(6348), 303–306 (2017).
16. H. Liu, Y. Li, Y. S. You, S. Ghimire, T. F. Heinz, and D. A. Reis, "High-harmonic generation from an atomically thin semiconductor," Nat. Phys. **13**(3), 262–265 (2017).
17. N. Yoshikawa, K. Nagai, K. Uchida, Y. Takaguchi, S. Sasaki, Y. Miyata, and K. Tanaka, "Interband resonant high-harmonic generation by valley polarized electron–hole pairs," Nat. Commun. **10**(1), 3709 (2019).
18. Y. Kobayashi, C. Heide, H. K. Kelardeh, A. Johnson, F. Liu, T. F. Heinz, D. A. Reis, and S. Ghimire, "Polarization Flipping of Even-Order Harmonics in Monolayer Transition-Metal Dichalcogenides," Ultrafast Sci. **2021**, 1–9 (2021).
19. Z. Lou, Y. Zheng, C. Liu, L. Zhang, X. Ge, Y. Li, J. Wang, Z. Zeng, R. Li, and Z. Xu, "Ellipticity dependence of nonperturbative harmonic generation in few-layer MoS2," Opt. Commun. **469**, 125769 (2020).
20. Y. Bai, F. Fei, S. Wang, N. Li, X. Li, F. Song, R. Li, Z. Xu, and P. Liu, "High-harmonic generation from topological surface states," Nat. Phys. **17**(3), 311–315 (2021).
21. N. Yoshikawa, T. Tamaya, and K. Tanaka, "High-harmonic generation in graphene enhanced by elliptically polarized light excitation," Science **356**(6339), 736–738 (2017).
22. H. A. Hafez, S. Kovalev, J.-C. Deinert, Z. Mics, B. Green, N. Awari, M. Chen, S. Germanskiy, U. Lehnert, and J. Teichert, "Extremely efficient terahertz high-harmonic generation in graphene by hot Dirac fermions," Nature **561**(7724), 507–511 (2018).
23. B. Cheng, N. Kanda, T. N. Ikeda, T. Matsuda, P. Xia, T. Schumann, S. Stemmer, J. Itatani, N. P. Armitage, and R. Matsunaga, "Efficient terahertz harmonic generation with coherent acceleration of electrons in the Dirac semimetal Cd 3 As 2," Phys. Rev. Lett. **124**(11), 117402 (2020).
24. Y.-Y. Lv, J. Xu, S. Han, C. Zhang, Y. Han, J. Zhou, S.-H. Yao, X.-P. Liu, M.-H. Lu, and H. Weng, "High-harmonic generation in Weyl semimetal β-WP2 crystals," Nat. Commun. **12**(1), 6437 (2021).
25. J. Itatani, J. Levesque, D. Zeidler, H. Niikura, H. Pépin, J. C. Kieffer, P. B. Corkum, and D. M. Villeneuve, "Tomographic imaging of molecular orbitals," Nature **432**(7019), 867–871 (2004).
26. P. B. Corkum and F. Krausz, "Attosecond science," Nat. Phys. **3**(6), 381–387 (2007).
27. H. J. Wörner, J. B. Bertrand, D. V. Kartashov, P. B. Corkum, and D. M. Villeneuve, "Following a chemical reaction using high-harmonic interferometry," Nature **466**(7306), 604–607 (2010).
28. P. Lan, M. Ruhmann, L. He, C. Zhai, F. Wang, X. Zhu, Q. Zhang, Y. Zhou, M. Li, M. Lein, and P. Lu, "Attosecond Probing of Nuclear Dynamics with Trajectory-Resolved High-Harmonic Spectroscopy," Phys. Rev. Lett. **119**(3), 033201 (2017).
29. O. Schubert, M. Hohenleutner, F. Langer, B. Urbanek, C. Lange, U. Huttner, D. Golde, T. Meier, M. Kira, and S. W. Koch, "Sub-cycle control of terahertz high-harmonic generation by dynamical Bloch oscillations," Nat. Photonics **8**(2), 119–123 (2014).
30. Y. W. Kim, T.-J. Shao, H. Kim, S. Han, S. Kim, M. Ciappina, X.-B. Bian, and S.-W. Kim, "Spectral interference in high harmonic generation from solids," ACS Photonics **6**(4), 851–857 (2019).
31. Z. Wang, H. Park, Y. H. Lai, J. Xu, C. I. Blaga, F. Yang, P. Agostini, and L. F. DiMauro, "The roles of photo-carrier doping and driving wavelength in high harmonic generation from a semiconductor," Nat. Commun. **8**(1), 1686 (2017).
32. P. Ye, X. He, H. Teng, M. Zhan, S. Zhong, W. Zhang, L. Wang, and Z. Wei, "Full Quantum Trajectories Resolved High-Order Harmonic Generation," Phys. Rev. Lett. **113**(7), 073601 (2014).
33. G. Vampa, C. R. McDonald, G. Orlando, P. B. Corkum, and T. Brabec, "Semiclassical analysis of high harmonic generation in bulk crystals," Phys. Rev. B **91**(6), 064302 (2015).
34. M. Schultze, K. Ramasesha, C. D. Pemmaraju, S. A. Sato, D. Whitmore, A. Gandman, S. Prell James, L. J. Borja, D. Prendergast, K. Yabana, M. Neumark Daniel, and R. Leone Stephen, "Attosecond band-gap dynamics in silicon," Science **346**(6215), 1348–1352 (2014).

Optics EXPRESS

35. C. Heide, Y. Kobayashi, A. C. Johnson, F. Liu, T. F. Heinz, D. A. Reis, and S. Ghimire, "Probing electron-hole coherence in strongly driven 2D materials using high-harmonic generation," Optica **9**(5), 512–516 (2022).
36. L. Yue and M. B. Gaarde, "Imperfect recollisions in high-harmonic generation in solids," Phys. Rev. Lett. **124**(15), 153204 (2020).
37. X.-Q. Wang, Y. Xu, X.-H. Huang, and X.-B. Bian, "Interference between inter-and intraband currents in high-order harmonic generation in solids," Phys. Rev. A **98**(2), 023427 (2018).
38. R. Zuo, A. Trautmann, G. Wang, W.-R. Hannes, S. Yang, X. Song, T. Meier, M. Ciappina, H. T. Duc, and W. Yang, "Neighboring Atom Collisions in Solid-State High Harmonic Generation," Ultrafast Sci. **2021**, 1–8 (2021).
39. Y.-T. Zhao, S.-C. Jiang, X. Zhao, J.-G. Chen, and Y.-J. Yang, "Effect of interband polarization on a solid's high-order-harmonic generation just belowthe band gap," Opt. Lett. **45**(10), 2874–2877 (2020).
40. G. Vampa, T. J. Hammond, N. Thiré, B. E. Schmidt, F. Légaré, C. R. McDonald, T. Brabec, and P. B. Corkum, "Linking high harmonics from gases and solids," Nature **522**(7557), 462–464 (2015).
41. X. Song, R. Zuo, S. Yang, P. Li, T. Meier, and W. Yang, "Attosecond temporal confinement of interband excitation by intraband motion," Opt. Express **27**(3), 2225–2234 (2019).
42. A. A. Lanin, E. A. Stepanov, A. B. Fedotov, and A. M. Zheltikov, "Mapping the electron band structure by intraband high-harmonic generation in solids," Optica **4**(5), 516–519 (2017).
43. T. T. Luu and H. J. Wörner, "Measurement of the Berry curvature of solids using high-harmonic spectroscopy," Nat. Commun. **9**(1), 916 (2018).
44. H. Lakhotia, H. Y. Kim, M. Zhan, S. Hu, S. Meng, and E. Goulielmakis, "Laser picoscopy of valence electrons in solids," Nature **583**(7814), 55–59 (2020).
45. L. Li, P. Lan, L. He, W. Cao, Q. Zhang, and P. Lu, "Determination of electron band structure using temporal interferometry," Phys. Rev. Lett. **124**(15), 157403 (2020).
46. C. Qian, C. Yu, S. Jiang, T. Zhang, J. Gao, S. Shi, H. Pi, H. Weng, and R. Lu, "Role of Shift Vector in High-Harmonic Generation from Noncentrosymmetric Topological Insulators under Strong Laser Fields," Phys. Rev. X **12**, 021030 (2022).
47. G. Vampa, C. R. McDonald, G. Orlando, D. D. Klug, P. B. Corkum, and T. Brabec, "Theoretical analysis of high-harmonic generation in solids," Phys. Rev. Lett. **113**(7), 073901 (2014).
48. X. He, J. M. Dahlström, R. Rakowski, C. M. Heyl, A. Persson, J. Mauritsson, and A. L'Huillier, "Interference effects in two-color high-order harmonic generation," Phys. Rev. A **82**(3), 033410 (2010).
49. C. Q. Abadie, M. Wu, and M. B. Gaarde, "Spatiotemporal filtering of high harmonics in solids," Opt. Lett. **43**(21), 5339–5342 (2018).
50. L. Yue and M. B. Gaarde, "Introduction to theory of high-harmonic generation in solids: tutorial," J. Opt. Soc. Am. B **39**(2), 535–555 (2022).
51. T. T. Luu, M. Garg, S. Y. Kruchinin, A. Moulet, M. T. Hassan, and E. Goulielmakis, "Extreme ultraviolet high-harmonic spectroscopy of solids," Nature **521**(7553), 498–502 (2015).
52. M. Hussain, S. Kaassamani, T. Auguste, W. Boutu, D. Gauthier, M. Kholodtsova, J. T. Gomes, L. Lavoute, D. Gaponov, and N. Ducros, "Spectral control of high order harmonics through non-linear propagation effects," Appl. Phys. Lett. **119**(7), 071101 (2021).
53. J.-B. Li, X. Zhang, S.-J. Yue, H.-M. Wu, B.-T. Hu, and H.-C. Du, "Enhancement of the second plateau in solid high-order harmonic spectra by the two-color fields," Opt. Express **25**(16), 18603–18613 (2017).
54. G. Vampa, T. J. Hammond, N. Thiré, B. E. Schmidt, F. Légaré, C. R. McDonald, T. Brabec, D. D. Klug, and P. B. Corkum, "All-Optical Reconstruction of Crystal Band Structure," Phys. Rev. Lett. **115**(19), 193603 (2015).
55. J. Tan, S. Xu, X. Han, Y. Zhou, M. Li, W. Cao, Q. Zhang, and P. Lu, "Resolving and weighing the quantum orbits in strong-field tunneling ionization," Adv. Photonics **3**(3), 035001 (2021).

Web of Science™ Core Collection

经检索《Web of Science™ Core Collection》，下述论文被《SCI - Expanded》收录。（数据获取：2023年03月13日）

标题:Trajectory-controlled high-order harmonic generation in ZnO crystals

作者:Wang, Y(Wang, Yang) Shao, TJ(Shao, Tianjiao) Li, XF(Li, Xiaofang) Liu, Y(Liu, Yu) Jiang, PZ(Jiang, Pengzuo) Zheng, W(Zheng, Wei) Zhang, LF(Zhang, Linfeng) Bian, XB(Bian, Xuebin) Liu, YQ(Liu, Yunquan) Gong, QH(Gong, Qihuang) Wu, CY(Wu, Chengyin)

来源出版物:OPTICS EXPRESS **卷**:31 **期**:2 **页**:3379-3389

出版时间:2023,JAN 16 **DOI**:10.1364/OE.481744

出版商:Optica Publishing Group **出版商地址**:2010 MASSACHUSETTS AVE NW, WASHINGTON, DC 20036 USA

文献类型:Article **语种**:English

入藏号:WOS:000921618900206 **IDS号**:8I3IN

地址:[Wang, Yang; Li, Xiaofang; Liu, Yu; Jiang, Pengzuo; Zheng, Wei; Zhang, Linfeng; Liu, Yunquan; Gong, Qihuang; Wu, Chengyin] Peking Univ, State Key Lab Mesoscop Phys, Sch Phys, Beijing 100871, Peoples R China; [Wang, Yang; Li, Xiaofang; Liu, Yu; Jiang, Pengzuo; Zheng, Wei; Zhang, Linfeng; Liu, Yunquan; Gong, Qihuang; Wu, Chengyin] Peking Univ, Frontiers Sci Ctr Nanooptoelect, Sch Phys, Beijing 100871, Peoples R China; [Shao, Tianjiao] NingboTech Univ, Sch Informat Sci & Engn, Ningbo 315100, Peoples R China; [Bian, Xue-Bin] Chinese Acad Sci, Innovat Acad Precis Measurement Sci & Technol, Wuhan Inst Phys & Math, State Key Lab Magnet Resonance & Atom & Mol Phys, Wuhan 430071, Peoples R China; [Liu, Yunquan; Gong, Qihuang; Wu, Chengyin] Collaborat Innovat Ctr Quantum Matter, Beijing 100871, Peoples R China; [Liu, Yunquan; Gong, Qihuang; Wu, Chengyin] Shanxi Univ, Collaborat Innovat Ctr Extreme Opt, Taiyuan 030006, Shanxi, Peoples R China; [Liu, Yunquan; Gong, Qihuang; Wu, Chengyin] Peking Univ, Yangtze Delta Inst Optoelect, Nantong 226010, Jiangsu, Peoples R China

通讯作者:Wu, CY (corresponding author), Peking Univ, State Key Lab Mesoscop Phys, Sch Phys, Beijing 100871, Peoples R China.; Wu, CY (corresponding author), Peking Univ, Frontiers Sci Ctr Nanooptoelect, Sch Phys, Beijing 100871, Peoples R China.; Shao, TJ (corresponding author), NingboTech Univ, Sch Informat Sci & Engn, Ningbo 315100, Peoples R China.; Bian, XB (corresponding author), Chinese Acad Sci, Innovat Acad Precis Measurement Sci & Technol, Wuhan Inst Phys & Math, State Key Lab Magnet Resonance & Atom & Mol Phys, Wuhan 430071, Peoples R China.; Wu, CY (corresponding author), Collaborat Innovat Ctr Quantum Matter, Beijing 100871, Peoples R China.; Wu, CY (corresponding author), Shanxi Univ, Collaborat Innovat Ctr Extreme Opt, Taiyuan 030006, Shanxi, Peoples R China.; Wu, CY (corresponding author), Peking Univ, Yangtze Delta Inst Optoelect, Nantong 226010, Jiangsu, Peoples R China.

电子邮件:shaotj@nit.zju.edu.cn; xuebin.bian@wipm.ac.cn; cywu@pku.edu.cn

ISSN:1094-4087

ISO 来源文献缩写:Opt. Express **来源出版物页码计数**:11

注：

以上检索结果均得到被检索人的确认。本证明编号：NBT-SCIE-2023-5288

《SCI - Expanded》检索结果（收录情况）

浙大宁波理工学院图书馆

检索人(签名):

审核人(签章):

2023年06月09日

InCites™ Journal Citation Reports®

经检索《Web of Science™》的JCR数据库，期刊《OPTICS EXPRESS》2021年JCR的影响因子情况：

ISSN：1094-4087

2021年影响因子：3.833

OPTICS：Q1

注：

1.以上检索结果均得到被检索人的确认。证明编号：NBT-SCIE-2023-5288-IF2021

2.论文的期刊影响因子应与该论文所发表期刊的年份相对应。

3.因JCR的最新数据截至到2021年，2023年出版论文的期刊影响因子以2021年的期刊影响因子为参考。

《JOURNAL CITATION REPORTS（JCR）》检索结果

浙大宁波理工学院图书馆

检索人(签名)：

审核人(签章)：

2023年06月09日